J. Fluid Mech. (2006), *vol.* 546, *pp.* 341–362.
doi:10.1017/S0022112005007123 Printed in the United Kingdom

Analytical and numerical study of the near flow field and shape of the Mach stem in steady flows

By LIAN-HUA TAN, YU-XIN REN AND ZI-NIU WU†

Department of Engineering Mechanics, Tsinghua University, Beijing 100084, P. R. China

(Received 19 March 2005 and in revised form 6 July 2005)

The flow fields behind the Mach stem in steady-state Mach reflections are analysed theoretically and numerically. When the angle between the slipline and the reflecting plane is sufficiently small, the subsonic flow just behind the Mach stem can be described by the isentropic small-disturbance equation. Using this analytical model, a very simple algebraic expression for the shape of the Mach stem is obtained. It is found that the Mach stem is well-approximated by a circular arc with very small curvature. The prediction by the model agrees very well with numerical computations.

1. Introduction

It is well-known that the reflection of oblique shock waves in steady flows results in two types of wave configurations: regular reflection (RR) and Mach reflection (MR) (see figure 1). In RR, the incident shock wave (i) and the reflected shock wave (r) meet at the reflecting surface to form a two-shock configuration at the reflection point. In MR, an additional shock wave, known as the Mach stem (M), connects the incident shock wave and reflected shock wave to form a triple-shock configuration.

Since Mach (1878) observed Mach reflection, a variety of problems have been addressed. Von Neumann (1945) developed the three-shock theory for MR. The search for the transition criterion from RR to MR or vice versa has been an objective of numerous studies. Von Neumann (1943) proposed two criteria for the transition from RR to MR: the detachment criterion and the mechanical equilibrium criterion. The latter was reinitiated by Henderson & Lozzi (1975) and was called the von Neumann criterion. In the (M_∞, θ_w)-plane (figure 2), where M_∞ is the free-stream Mach number and θ_w is the wedge angle, the detachment criterion and the von Neumann criterion are represented by two distinct curves: the von Neumann criterion is represented by the lower curve ($\theta_w = \theta_w^N(M_\infty)$), below which only RR is possible, and the detachment criterion is represented by the upper curve ($\theta_w = \theta_w^D(M_\infty)$), above which only MR is possible. The domain between these two curves is called the dual solution domain. In recent years, experimental and theoretical studies (Henderson & Lozzi 1979; Hornung & Robinson 1982; Teshukov 1989; Li & Ben-Dor 1996; Chpoun *et al.* 1994, 1995; Vuillon, Zeitoun & Ben-Dor 1995) have shown that both RR and MR are possible in the dual solution domain. The existence of a dual solution domain led Hornung, Oertel & Sandeman (1979) to hypothesize that a hysteresis could exist in the RR $\longleftrightarrow$ MR transition process. Chpoun *et al.* (1995) were the first to record hysteresis in the RR $\longleftrightarrow$ MR transition experimentally. Chpoun *et al.* (1994) and Ivanov, Gimelshein & Beylich (1995) confirmed the existence of this hysteresis through

† Corresponding author, Email: ziniuwu@tsinghua.edu.cn

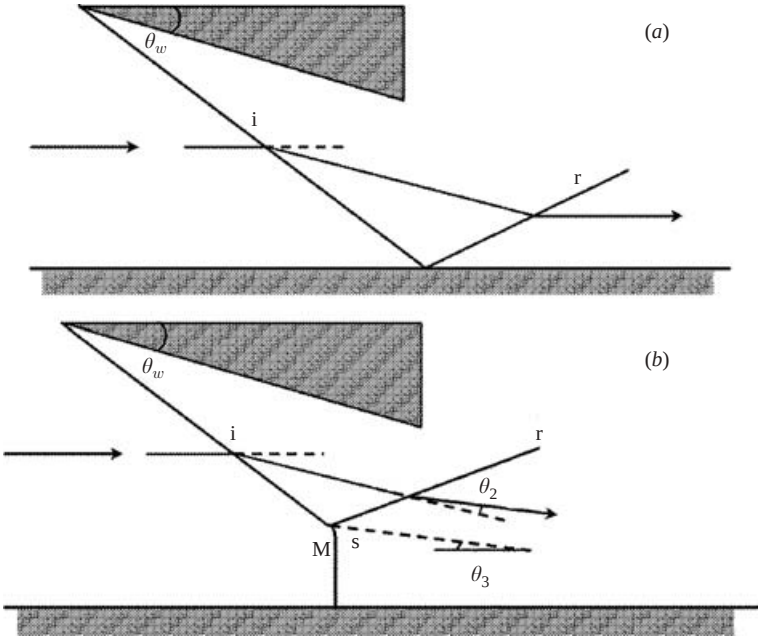

FIGURE 1. Shock wave reflections. (*a*) Regular reflection, (*b*) Mach reflection.

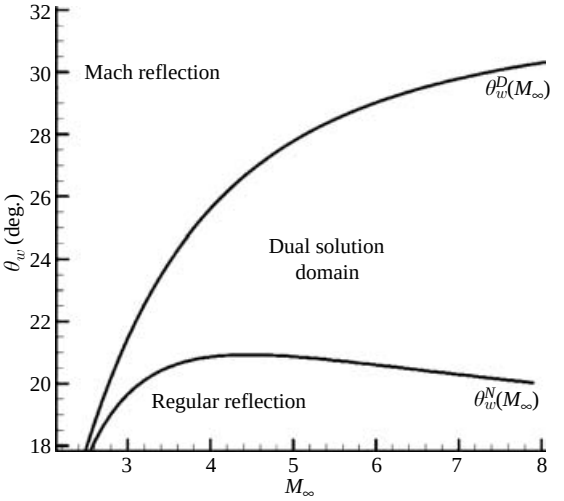

FIGURE 2. Domains of different types of reflection.

numerical experiments. Both wedge-angle-variation-induced hysteresis and Mach-number-variation-induced hysteresis are possible. Fomin *et al.* (1996) and Skews (1997, 2000) showed that the hysteresis details were contaminated by three-dimensional effect and therefore could not be considered as purely two-dimensional. Ben-dor, Elperin & Vasiliev (2003) studied flow Mach-number-variation-induced hysteresis for conical shock waves. More details of shock wave reflections can be found in Ben-Dor (1991), Ben-Dor, Igra & Elperin (2001), and Ben-Dor *et al.* (2002).

Understanding the characteristics of the Mach stem is important in the design of supersonic vehicles. Li & Ben-Dor (1997) used several examples to show the great

influence of the Mach stem geometry on the operating conditions of the inlet/combustor of a hypersonic craft, on the heating loads of a blunt body, and on the initiation of the detonation in a ram accelerator. However, after Courant & Friedrichs (1948) raised the question of how to determine the size of the Mach reflection, further analytical studies were not conducted until the 1990s. Azevedo & Liu (1993) proposed an engineering approach to estimate the height and location of the Mach stem. Li & Ben-Dor (1997) performed a more elaborated study for the flow fields associated with Mach reflection. Their analytical model is used to identify the dominant factors that affect the size and location of Mach reflections in certain steady flow situations. They noted that the centred expansion fan that originated at the trailing edge of the wedge interacted with the slipline to create the sonic throat and hence determined the Mach stem height and location.

In this paper, we will perform a detailed analysis of the subsonic flow pocket just behind the Mach stem by assuming the angle between the slipline and the reflecting plane to be sufficiently small. Specifically, we will study the shape of the Mach stem. It is interesting to note that there have been some experimental studies concerning the shape of the Mach stem for pseudo-steady reflections. Dewey & McMillin (1985*a*, *b*) made a detailed study of the shapes of the incident, reflected and Mach stem shocks. They showed that the Mach stem was described well by a circular arc, although the centre of the Mach stem was slightly below the reflecting surface. Their experimental results were confirmed by Olim & Dewey (1992) and Dewey & Barss (1996). The shape of the Mach stem has also been studied analytically by Li, Ben-Dor & Han (1994) for pseudo-steady reflections, and by Li & Ben-Dor (1997) for steady flows from a geometrical point of view.

The analytical model suitable for describing the steady subsonic flow just behind the Mach stem will be presented in § 2. The orders of some disturbance flow variables in this subsonic flow pocket will be first analysed in detail to obtain the correct flow model. Based on this analysis, the small-disturbance flow model valid in this region will be derived. In § 3, the governing equation for the flow model § 2 will be solved and an analytical expression for the shape of the Mach stem will be obtained. In § 4, numerical case studies will be performed to verify the analytical results. The essential points of this paper will be summarized in § 5.

2. Analysis of the flow field and the flow model for the subsonic flow pocket just behind the Mach stem

2.1. *Basic assumptions*

Figure 3 shows an example of Mach reflection. For the chosen coordinate system, x lies along the reflecting surface and y is perpendicular to this surface. The triple point is on the y-axis. The height of the Mach stem H_m is assumed to be known, either experimentally, numerically, or analytically using the model developed by Li & Ben-Dor (1997).

The basic assumption adopted in the analysis is that θ_3, the angle between the slipline s and the horizontal surface measured in radians, is small, namely $\theta_3 \sim \epsilon$, where ϵ is a small quantity. Using the three-shock theory, we can calculate the value of θ_3 for a wide range of incoming flow-Mach number M_∞ and wedge angle θ_w. Figure 4 displays the result for the parameter range $M_\infty = 3.0 \sim 5.0$ and $\theta_w = 21^\circ \sim 28^\circ$. It is clear that $\theta_3 < 12^\circ$ (0.209 rad) over the specified range of M_∞ except near the upper left corner. Thus, the small angle assumption is not as restrictive as it appears.

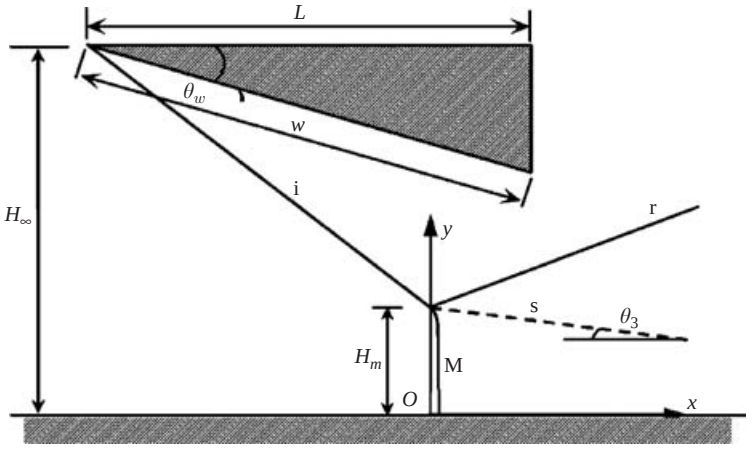

FIGURE 3. Mach reflection.

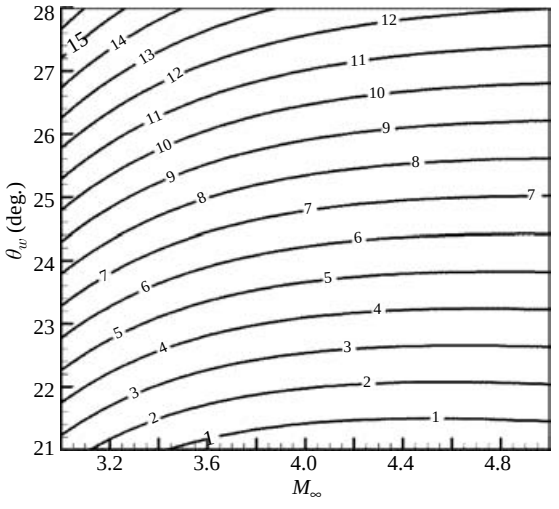

FIGURE 4. Diagram of $\theta_3 = \theta_3(M_\infty, \theta_w)$.

2.2. *Features of flows in the subsonic pocket just behind the Mach stem*

We use subscript ∞ to denote the flow condition before the Mach stem, and 0 to denote the flow condition downstream of the lowest point of the Mach stem. Then we can express the velocity components V_x, V_y, the pressure P, the temperature T and the entropy S in the subsonic pocket as the sum of a constant-state solution and a small perturbation:

$$
\begin{aligned}
V_x &= V_0 + v_x, \\
V_y &= v_y, \\
P &= P_0 + p, \\
T &= T_0 + t, \\
S &= S_0 + s.
\end{aligned}
$$

We first assume the flow to be rotational and express the perturbation of the velocity as the sum of a potential part and a rotational part:

$$v_x = \frac{\partial \phi}{\partial x} + m_x, \quad v_y = \frac{\partial \phi}{\partial y}, \tag{1}$$

where m_x represents the contribution from the rotational part. It can be shown that adding a similar term, say m_y, in the expression for v_y does not affect the results, since we can make a transformation to eliminate this term.

We only consider the flow in the subsonic pocket sufficiently close to Mach stem. The analytical results obtained in the following paragraphs are strictly valid only in a very narrow band behind the Mach stem. However, this is enough for us to determine the shape of Mach stem.

The orders of the perturbation variables will be related to the small quantity $\theta_3 \sim \epsilon$ or θ. It is obvious that $\theta \lesssim O(\epsilon)$. To avoid cumbersome notation, we simply write

$$\theta \sim O(\epsilon). \tag{2}$$

2.2.1. *The entropy field*

The difference between the entropy after and before the Mach stem can be found from any classical textbooks on gas dynamics:

$$S - S_\infty = Rf(\beta),$$

where

$$f(\beta) = \ln \left\{ \left[1 + \frac{2\gamma}{\gamma+1} \left(M_\infty^2 \sin^2 \beta - 1 \right) \right]^{1/(\gamma-1)} \left[\frac{(\gamma+1) M_\infty^2 \sin^2 \beta}{(\gamma-1) M_\infty^2 \sin^2 \beta + 2} \right]^{-\gamma/(\gamma-1)} \right\},$$

and β is the local shock angle, i.e. the angle between the tangent of the (local) shock front of the Mach stem and the x-axis. At the lowest point of the Mach stem, we have $\beta = \pi/2$ and $S = S_0$.

From the theory of oblique shock waves, we have

$$\tan \theta = 2 \frac{\cos \beta}{\sin \beta} \frac{M_\infty^2 \sin^2 \beta - 1}{M_\infty^2 (\gamma + \cos 2\beta) + 2}, \tag{3}$$

which along with (2) leads to

$$\beta - \pi/2 \sim \theta \sim O(\epsilon). \tag{4}$$

Expanding $f(\beta)$ about $\pi/2$, we obtain

$$f(\beta) = f\left(\frac{\pi}{2}\right) + f'\left(\frac{\pi}{2}\right)\left(\beta - \frac{\pi}{2}\right) + \frac{1}{2} f''\left(\frac{\pi}{2}\right)\left(\beta - \frac{\pi}{2}\right)^2 + \cdots.$$

It is easy to show that $f'(\pi/2) = 0$. Hence the entropy perturbation defined by $s = S - S_0$ is given by

$$s = R\left[f\left(\beta\right) - f\left(\frac{\pi}{2}\right) \right] = R\left[\frac{1}{2} f''\left(\frac{\pi}{2}\right)\left(\beta - \frac{\pi}{2}\right)^2 + \cdots \right]. \tag{5}$$

Inserting (4) into the above expression yields

$$s \sim O(\epsilon^2). \tag{6}$$

Hence, the entropy perturbation is of second order.

Using (5), we obtain

$$\frac{\partial s}{\partial \beta} = Rf''\left(\frac{\pi}{2}\right)\left(\beta - \frac{\pi}{2}\right) + \cdots = O(\epsilon)$$

so that the following expression holds:

$$\frac{\partial s}{\partial y} = \frac{\partial s}{\partial \beta}\frac{\partial \beta}{\partial y} \sim \frac{\partial \beta}{\partial y} O(\epsilon). \tag{7}$$

There is no need to know the exact order of $\partial\beta/\partial y$ in the subsequent analysis. We simply write

$$\frac{\partial \beta}{\partial y} \sim O(\epsilon^k), \tag{8}$$

with $k \geqslant 0$. Therefore, we have from (7)

$$\frac{\partial s}{\partial y} \sim O(\epsilon^{1+k}). \tag{9}$$

Using the well-known Crocco's theorem $\boldsymbol{V} \times \boldsymbol{\Omega} = -T\nabla S$, we can write

$$V_x \Omega_z = T\frac{\partial S}{\partial y}, \quad V_y \Omega_z = -T\frac{\partial S}{\partial x},$$

where $\boldsymbol{\Omega}$ denotes the vorticity. Neglecting the smaller terms, we have

$$\Omega_z = \frac{T_0}{V_0}\frac{\partial s}{\partial y} = -\frac{T_0}{v_y}\frac{\partial s}{\partial x}. \tag{10}$$

In § 2.2.2, we will show that $v_y \sim O(\epsilon)$; therefore, we have

$$\frac{\partial s}{\partial x} = \frac{v_y}{V_0}\frac{\partial s}{\partial y} \sim O(\epsilon^{2+k}). \tag{11}$$

In summary, the entropy perturbation in the subsonic flow region just behind the Mach stem satisfies the following order of magnitude estimations:

$$s \sim O(\epsilon^2), \qquad \frac{\partial s}{\partial x} \sim O(\epsilon^{2+k}), \qquad \frac{\partial s}{\partial y} \sim O(\epsilon^{1+k}). \tag{12}$$

2.2.2. *The velocity perturbation*

The flow angle θ is related to the velocity by the expression $\tan\theta = -v_y/(V_0 + v_x)$, which can be approximated by

$$\theta \cong -\frac{v_y}{V_0}. \tag{13}$$

This means that

$$v_y \sim O(\epsilon),$$

since $\theta \sim O(\epsilon)$.

For small θ, (3) gives

$$\theta = \alpha \cos\beta, \quad \alpha = \frac{2\left(M_\infty^2 - 1\right)}{2 + (\gamma - 1)M_\infty^2}. \tag{14}$$

The pressure across the Mach stem satisfies

$$\frac{P}{P_\infty} = 1 + \frac{2\gamma}{\gamma + 1}\left(M_\infty^2 \sin^2\beta - 1\right). \tag{15}$$

At the lowest point of the Mach stem, we have $\beta = \pi/2$ and $P|_{y=0} = P_0$ so that

$$\frac{P_0}{P_\infty} = 1 + \frac{2\gamma}{\gamma+1}\left(M_\infty^2 - 1\right). \tag{16}$$

Using (14) to (16), the pressure perturbation behind the Mach stem is calculated to be

$$\frac{p}{P_\infty} = -\frac{2\gamma}{\gamma+1} M_\infty^2 \cos^2\beta = -\frac{2\gamma}{\gamma+1} M_\infty^2 \frac{\theta^2}{\alpha^2}. \tag{17}$$

Since $\alpha \sim O(1)$, for sufficiently large $M_\infty^2 - 1$, we have

$$\frac{p}{P_\infty} \sim O(\varepsilon^2).$$

Using the following well-known expression for the linearized pressure coefficient:

$$\frac{p}{\frac{1}{2}\rho_0 V_0^2} = -2\frac{v_x}{V_0},$$

we obtain from (17) the following expressions for v_x:

$$v_x = \frac{K}{a_\infty}\theta^2, \quad K = \frac{\gamma+1}{2\left(M_\infty^2 - 1\right)^2}.$$

For large values of $M_\infty^2 - 1$, we have $K \sim O(1)$. Therefore

$$v_x \sim O(\epsilon^2). \tag{18}$$

From (18) it is clear that $\partial v_x/\partial x$ is at most of $O(\epsilon)$. Using a quasi-one-dimensional analysis, we can show that $\partial v_x/\partial x$ is just of $O(\epsilon)$. The averaged x-component velocity perturbation is denoted by $\bar{u}$ (averaged along the height of the slipline). We thus have $\partial v_x/\partial x \sim \partial \bar{u}/\partial x$ and

$$\frac{\mathrm{d}\bar{u}}{V_0} = -\frac{1}{1 - M_0^2}\frac{\mathrm{d}H}{H},$$

where H is the height of the slipline. Using this relation, it is easy to show that

$$\frac{\mathrm{d}\bar{u}}{\mathrm{d}x} = -\frac{V_0}{\left(1 - M_0^2\right)H}\frac{\mathrm{d}H}{\mathrm{d}x} \approx \frac{V_0}{\left(1 - M_0^2\right)H}\theta_3 \sim O(\epsilon),$$

and thus,

$$\frac{\partial v_x}{\partial x} \sim O(\epsilon). \tag{19}$$

For the rotational part of the velocity disturbance m_x, we substitute (2) into (10) to obtain

$$-\frac{\partial m_x}{\partial y} = \frac{T_0}{V_0}\frac{\partial s}{\partial y}.$$

Integrating this equation, we have

$$m_x = -\frac{T_0}{V_0}s + \eta(x). \tag{20}$$

Since the reflecting surface is a streamline, we necessarily have $\partial s/\partial x|_{y=0} = 0$. Since the reflecting surface is also a symmetry line, we have $\partial s/\partial y|_{y=0} = 0$. This means that $\nabla s|_{y=0} = 0$, i.e. the flow is irrotational on the reflecting plane behind the Mach stem

and the following expression holds:

$$m_x|_{y=0} = 0.$$

Using this relation and $s|_{y=0} = 0$ in (20), we obtain $\eta(x) = 0$ so that (20) reduces to

$$m_x = -\frac{T_0}{V_0} s \sim O(\epsilon^2). \tag{21}$$

2.3. *The flow model in the subsonic pocket just behind the Mach stem*

Shapiro (1953, p. 266) noted that, when shocks appear in an initially irrotational flow, the flow downstream of the shock is in general rotational. However, the amount of rotation introduced by a curved shock is often so small that there is little error in treating the downstream flow as irrotational. Here we prove that the flow just behind the Mach stem can indeed be described by the potential flow equation. Inserting (2) into the small-perturbation equation

$$\left(1 - M_0^2\right) \frac{\partial v_x}{\partial x} + \frac{\partial v_y}{\partial y} = 0,$$

and using (21) to eliminate m_x, we obtain

$$\left(1 - M_0^2\right) \left(\frac{\partial^2 \phi}{\partial x^2} - \frac{T_0}{V_0} \frac{\partial s}{\partial x} \right) + \frac{\partial^2 \phi}{\partial y^2} = 0. \tag{22}$$

From (19), we have

$$\frac{\partial v_x}{\partial x} = \frac{\partial^2 \phi}{\partial x^2} - \frac{T_0}{V_0} \frac{\partial s}{\partial x} \sim O(\epsilon).$$

This means that $\partial s/\partial x$, which is of $O(\epsilon^{2+k})$ $(k \geqslant 0)$ according to (12), can be ignored. Hence the flow in the subsonic pocket just behind the Mach stem can be described by the potential flow equation

$$\left(1 - M_0^2\right) \frac{\partial^2 \phi}{\partial x^2} + \frac{\partial^2 \phi}{\partial y^2} = 0. \tag{23}$$

The normal velocity vanishes on the reflecting surface, implying

$$\left. \frac{\partial \phi}{\partial y} \right|_{y=0} = 0. \tag{24}$$

At the triple point, the velocity to the right of the Mach stem is in the same direction as the slipline

$$\left. \frac{\partial \phi}{\partial y} \right|_{y=H_m} = -V_0 \theta_3. \tag{25}$$

Neglecting the $O(\epsilon^2)$ term in (18), we obtain another condition

$$\left. \frac{\partial \phi}{\partial x} \right|_{x=0} = 0. \tag{26}$$

It should be noted that the flow behind the Mach stem is subsonic, and hence the downstream influence can theoretically reach the Mach stem. In order to obtain the complete solution in the subsonic pocket, we need a fourth boundary condition downstream of the subsonic region. However, in the present paper, we are interested in the shape of the Mach stem, which is related only to the asymptotic behaviour

of the solution just behind the Mach stem. For this purpose, the governing equation (23) and boundary conditions (24), (25), and (26) form a closed set.

3. Analytical expression for the shape of the Mach stem

3.1. *The solution of the small-disturbance equation*

We non-dimensionalize (23) according to

$$\bar{\phi} = \frac{\phi}{a_0 H_\infty}, \quad \bar{x} = \frac{x}{H_\infty}, \quad \bar{y} = \frac{y}{H_\infty}, \quad \bar{H}_m = \frac{H_m}{H_\infty},$$

where H_∞ is the distance between the leading edge of the wedge and the x-axis, and a_0 is the speed of sound downstream of the lowest point of the Mach stem. The non-dimensional isentropic small-disturbance equation can be written as

$$\kappa^2 \frac{\partial^2 \bar{\phi}}{\partial \bar{x}^2} + \frac{\partial^2 \bar{\phi}}{\partial \bar{y}^2} = 0, \tag{27}$$

where $\kappa^2 = 1 - M_0^2$. The non-dimensional boundary conditions (24), (25) and (26) are

$$\bar{y} = 0, \quad \frac{\partial \bar{\phi}}{\partial \bar{y}} = 0; \tag{28}$$

$$\bar{y} = \bar{H}_m, \quad \frac{\partial \bar{\phi}}{\partial \bar{y}} = -\frac{V_0 \theta_3}{a_0}; \tag{29}$$

$$\bar{x} = 0, \quad \frac{\partial \bar{\phi}}{\partial \bar{x}} = 0. \tag{30}$$

For $\bar{x} \ll 1$, we can expand $\bar{\phi}$ in terms of $\bar{x}$ as follows:

$$\bar{\phi} = f_0(\bar{y}) + f_1(\bar{y})\bar{x} + f_2(\bar{y})\bar{x}^2 + \cdots. \tag{31}$$

Neglecting the terms of order higher than $O(\bar{x}^2)$ in (31) and substituting the resulting expression into (27), we obtain

$$[2\kappa^2 f_2(\bar{y}) + f_0''(\bar{y})] + f_1''(\bar{y})\bar{x} + f_2''(\bar{y})\bar{x}^2 = 0. \tag{32}$$

Because (32) holds for all $\bar{x}$, we must have

$$2\kappa^2 f_2(\bar{y}) + f_0''(\bar{y}) = 0, \tag{33}$$

$$f_1''(\bar{y}) = 0, \tag{34}$$

$$f_2''(\bar{y}) = 0. \tag{35}$$

Inserting (31) in (28) to (30), we obtain the following expressions:

$$f_0'(0) = 0, \quad f_0'(\bar{H}_m) = -\frac{V_0 \theta_3}{a_0}, \tag{36}$$

$$f_2'(0) = 0, \quad f_2'(\bar{H}_m) = 0, \tag{37}$$

$$f_1(\bar{y}) = 0. \tag{38}$$

The solutions of (33) and (35), subjected to the boundary conditions (36) and (37), are

$$f_2(\bar{y}) = C_1, \tag{39}$$

$$f_0(\bar{y}) = -C_1 \kappa^2 \bar{y}^2 + C_2, \tag{40}$$

with

$$C_1 = \frac{V_0\theta_3}{2\kappa^2 a_0 \overline{H}_m}.$$

Substituting (38) to (40) into (31), we obtain the potential of the velocity perturbation

$$\overline{\phi} = C_2 + \frac{V_0\theta_3}{2a_0\overline{H}_m\kappa^2}\overline{x}^2 - \frac{V_0\theta_3}{2a_0\overline{H}_m}\overline{y}^2 + \cdots, \tag{41}$$

which results in

$$\overline{v}_x = \frac{V_0\theta_3}{a_0\overline{H}_m\kappa^2}\overline{x}, \quad \overline{v}_y = -\frac{V_0\theta_3}{a_0\overline{H}_m}\overline{y}.$$

In dimensional form, the expressions for the velocity are given by

$$v_x = \frac{V_0\theta_3}{H_m\left(1-M_0^2\right)}x = \frac{\left[(\gamma-1)M_\infty^2+2\right]\left[2\gamma M_\infty^2-(\gamma-1)\right]}{H_m(\gamma+1)^2\left(M_\infty^2-1\right)}a_\infty\theta_3 x, \tag{42}$$

$$v_y = \frac{V_0\theta_3}{H_m}y = -\frac{(\gamma-1)M_\infty^2+2}{\gamma+1}\frac{\theta_3}{H_m}a_\infty y, \tag{43}$$

where we have used the following expressions (from the normal shock wave theory):

$$V_0 = a_\infty\frac{(\gamma-1)M_\infty^2+2}{\gamma+1}, \quad M_0^2 = \frac{1+\frac{1}{2}(\gamma-1)M_\infty^2}{\gamma M_\infty^2-\frac{1}{2}(\gamma-1)}.$$

3.2. *The shape of the Mach stem*

Denoting the profile of the Mach stem as $f(x, y) = 0$, we have

$$\frac{\mathrm{d}y}{\mathrm{d}x} = -\tan\beta = -\frac{\sqrt{1-\cos^2\beta}}{\cos\beta}. \tag{44}$$

which, along with (14), yields the following equation:

$$\frac{\mathrm{d}y}{\mathrm{d}x} = -\frac{\sqrt{1-(\theta/\alpha)^2}}{\theta/\alpha}. \tag{45}$$

Since $\theta = (\theta_3/H_m)y$ according to (43) and (13), (45) can be rewritten as

$$\frac{\mathrm{d}y}{\mathrm{d}x} = -\frac{\sqrt{1-(\theta_3/(\alpha H_m))^2y^2}}{y(\theta_3/(\alpha H_m))}.$$

Integration of the above equation yields

$$(x+C)^2 + y^2 = \left(\frac{\alpha H_m}{\theta_3}\right)^2.$$

With $y|_{x=0} = H_m$, the constant C is determined to be $C = \sqrt{(\alpha H_m/\theta_3)^2 - H_m^2}$.

Therefore, the shape of the Mach stem is described by the curve

$$\left(x + \sqrt{\left(\frac{\alpha H_m}{\theta_3}\right)^2 - H_m^2}\right)^2 + y^2 = \left(\frac{\alpha H_m}{\theta_3}\right)^2, \tag{46}$$

with

$$\alpha = \frac{2\left(M_\infty^2-1\right)}{2+(\gamma-1)M_\infty^2}.$$

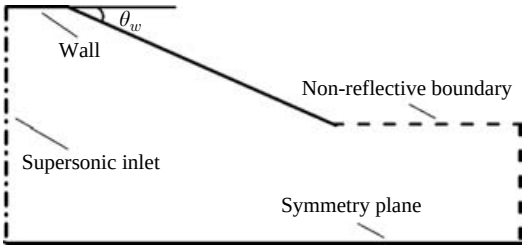

FIGURE 5. The computational domain and the boundary conditions.

It is clear that the shape of the Mach stem based on the present analysis is a circular arc centred at

$$\left(-\sqrt{\left(\frac{\alpha H_m}{\theta_3}\right)^2 - H_m^2}, 0\right),$$

and the two end points are $(0, H_m)$ and $(\alpha H_m/\theta_3 - \sqrt{(\alpha H_m/\theta_3)^2 - H_m^2}, 0)$. It should be noted that the centre of the circular arc is just on the reflecting plane.

4. Numerical validations and discussions

In this section, we will not only compare the numerical shape of the Mach stem with the analytical one, but also check some important order of magnitude estimations derived in § 2.

In the numerical simulation, we solve the full set of nonlinear Euler equations in gas dynamics using a Godunov-type flux-difference splitting method. In order to numerically capture the shape of the Mach stem, we will have to use a very fine grid. However, when the free-stream Mach number is large and/or the grid is fine enough, the 'carbuncle' or the 'odd-even decoupling' phenomena might occur (Quirk 1994) when a Godunov-type scheme is used. To avoid this difficulty, we use the rotated Riemann solver proposed by Ren (2003) which is free from the 'carbuncle' phenomena while capturing the slipline at high resolution.

We will choose a number of combinations of incoming-flow Mach number M_∞ and wedge angle θ_w to produce Mach reflection configurations with different θ_3 according to the three-shock theory. In figure 5, we display a typical computational domain and the types of boundary conditions used in the simulation. It should be noted that the configuration of the Mach reflection may be affected by the downstream boundary conditions under some circumstance, as being indicated by Henderson & Lozzi (1979), Hornung & Robinson (1982), and Li & Ben-Dor (1997). To isolate the Mach reflection from downstream influences in the numerical simulation, the flow conditions are chosen so that the flow field above slipline is supersonic everywhere. Furthermore, the outlet boundary is placed downstream of the sonic throat formed by the interaction between the expansion fan and the slipline. As a result, the flow is supersonic at the outlet (right) boundary and free of the far-field downstream influences.

There is no standard way to extract the shape of the Mach stem from numerical results. Due to the numerical viscosity, the computed discontinuities will spread over several ($1 \sim 3$) grid points. To overcome this difficulty, we extract the lines on which $|\nabla\rho|_L = 0.8|\nabla\rho|_{\max}$, where $|\nabla\rho|_{\max}$ is the maximum magnitude of the density gradient in the entire region covering the Mach stem. There are two contour lines on which

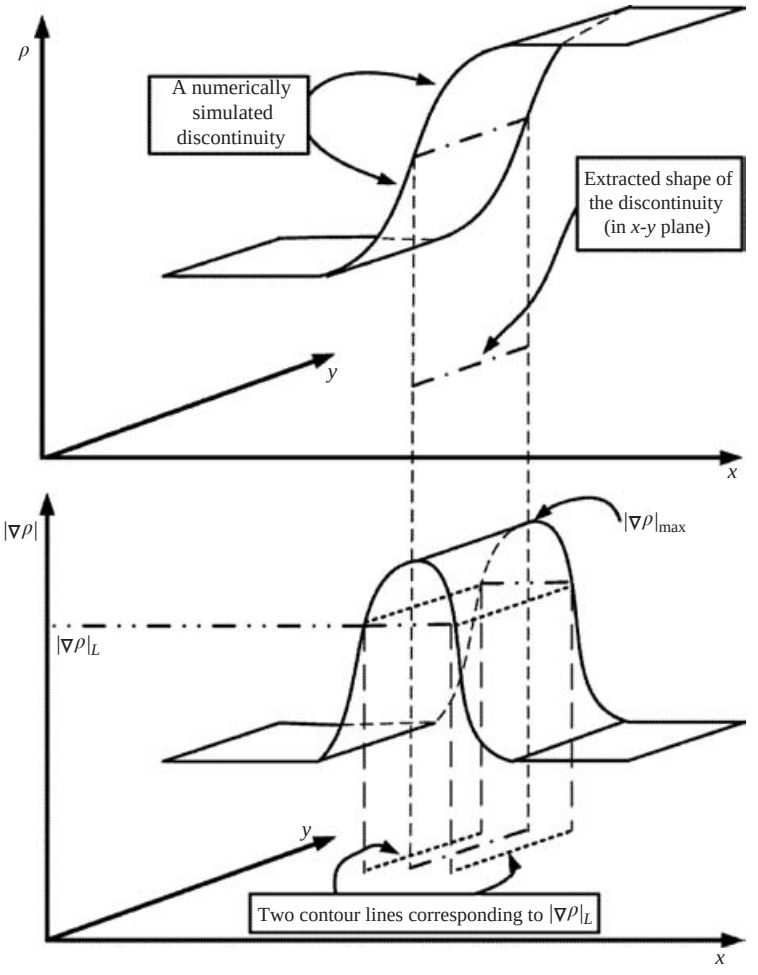

FIGURE 6. The procedure to determine the shape of a discontinuity from the numerical results.

$|\nabla\rho| = |\nabla\rho|_L$. The discontinuity is determined numerically by assuming it to be at the centre of these two lines. This procedure is illustrated in figure 6.

4.1. *The perturbation quantities in the subsonic pocket behind the Mach stem*

Recall that the flow model used in the derivation of the analytical shape of the Mach stem has been based on order of magnitude estimations like

$$s \sim O(\epsilon^2), \quad v_x \sim O(\epsilon^2), \quad v_y \sim O(\epsilon), \tag{47}$$

$$\frac{\partial s}{\partial x} \ll \frac{\partial s}{\partial y}, \tag{48}$$

which are obtained in § 2. Here we will validate these estimations numerically.

Consider the flow conditions $M_\infty = 3.0$, $\theta_w = 21.846^\circ$ and $w/H_\infty = 1.4$, where w is the diagonal length of the wedge. We use a 300×200 grid for numerical computation. The angle of the slip line is $\theta_3 = 4.20^\circ$ in this test case. We plot in figure 7 the distribution of normalized perturbation variables, denoted by $\hat{s}$, $\hat{v}_x$, and $\hat{v}_y$, along the vertical grid line that is nearest to the Mach stem in the subsonic pocket. The $\hat{s}$, $\hat{v}_x$, and $\hat{v}_y$

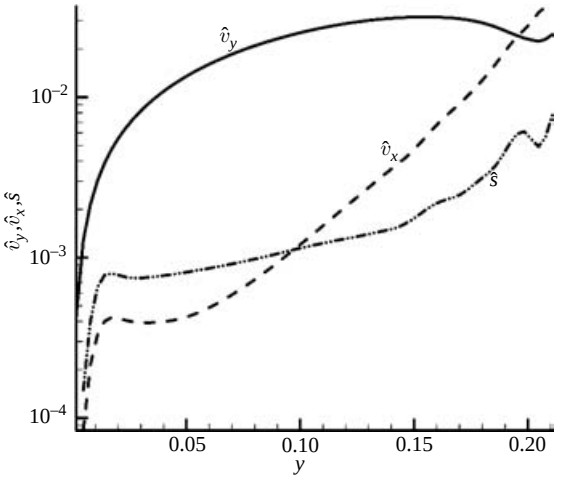

FIGURE 7. The distributions of $\hat{s}$, $\hat{v}_x$, and $\hat{v}_y$ along the vertical grid line that is nearest to the Mach stem in the subsonic pocket. $M_\infty = 3.0$, $\theta_w = 21.846°$, $\theta_3 = 4.20°$.

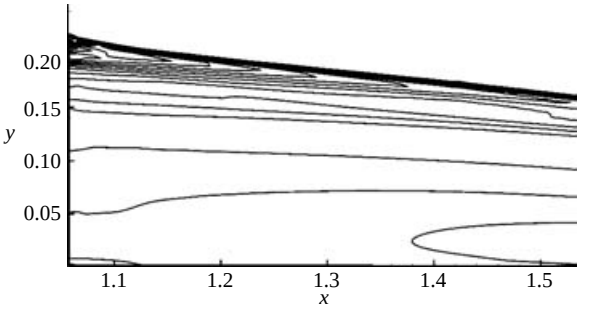

FIGURE 8. Contours of the entropy perturbation. $M_\infty = 3.0$, $\theta_w = 21.846°$.

are given by

$$\hat{s} = \frac{S - S_0}{V_0^2/T_0} = \frac{P_0}{(\gamma - 1)\rho_0 V_0^2} \ln\left[\left(\frac{P}{P_0}\right)\left(\frac{\rho_0}{\rho}\right)^\gamma\right],$$

$$\hat{v}_x = \frac{V_x - V_0}{V_0},$$

$$\hat{v}_y = \frac{V_y}{V_0},$$

where the expressions on the right-hand side of these equations are all obtained through numerical simulation, and the subscript 0 denotes variables on the reflecting surface. With the vertical axis in logarithmic scale, figure 7 clearly shows that $\hat{s}$ and $\hat{v}_x$ are approximately of the same order and are all about one order smaller than the quantity $\hat{v}_y$ for values of $y \leqslant 0.15$. This complies with the estimation of (47).

The contours of the entropy perturbation are illustrated in figure 8, which shows $\partial s/\partial x \ll \partial s/\partial y$. It is apparent that the contour lines of s are almost horizontal, validating the results of (48).

In deriving the irrotational equation in § 2.3, we have ignored $(T_0/V_0)\partial s/\partial x$ since we have shown that it is much smaller than $\partial v_x/\partial x$. To verify this, the computed

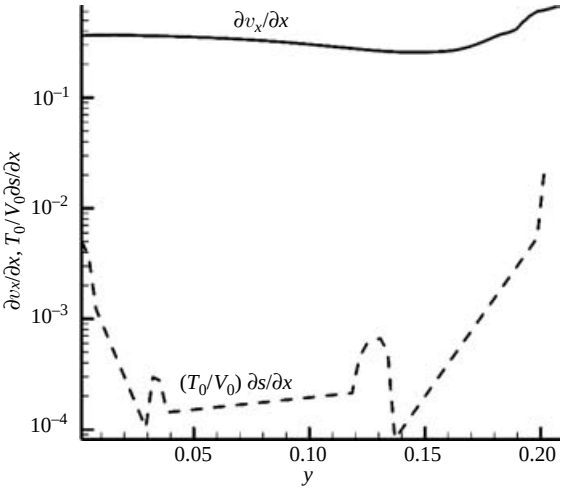

FIGURE 9. The comparison of the simulated $\partial v_x/\partial x$ and $(T_0/V_0)\partial s/\partial x$ along the vertical grid line that is nearest to the Mach stem in the subsonic pocket. $M_\infty = 3.0$, $\theta_w = 21.846°$, $\theta_3 = 4.20°$.

values for $\partial v_x/\partial x$ and $(T_0/V_0)\partial s/\partial x$ along the vertical grid line that is nearest to the Mach stem in the subsonic pocket are shown in figure 9, which clearly indicates that $(T_0/V_0)\partial s/\partial x$ is considerably smaller than $\partial v_x/\partial x$.

4.2. *The shape of the Mach stem*

Now we compare the numerical computation with the analytical expression (46) for the shape of the Mach stem. A grid refinement study is first performed. The flow conditions used for this study are $M_\infty = 4.96$, $\theta_w = 28°$ and $w/H_\infty = 1.1$. These conditions are taken from Shirozu & Nishida (1995) and are also used in Li & Ben-Dor (1997). Initially, an almost uniform 300×200 grid is used in the computation, and near the Mach stem the grid density in the x-direction is $\Delta x/L = 0.01$, where L is the horizontal length of the wedge. Different grid refinements are considered in a narrow strip containing the Mach stem by using $\Delta x/L = 0.005$, $\Delta x/L = 0.0025$ and $\Delta x/L = 0.00125$.

In figure 10, we display the shapes of simulated Mach stems in terms of the Mach number contours using different grid density as mentioned above. In figure 11, we show the Mach number contours using the grid with $\Delta x/L = 0.0025$. Figure 12 depicts the shapes of the Mach stem extracted from the numerical simulation. In figure 12, a clear trend of convergence in the shapes of the Mach stem can be seen. When the grid densities are $\Delta x/L = 0.0025$ and $\Delta x/L = 0.00125$, the shapes of the Mach stem are quite similar. However, for the $\Delta x/L = 0.00125$ grid, there are some 'wiggles' in its shape. These wiggles are due to the grid effect since the refinement is made only in the x-direction and the grid aspect ratio becomes very large in this case. In this sense, the grid with $\Delta x/L = 0.0025$ is more suitable for obtaining the simulated Mach stem shape. During the grid refinement, the predicted heights of the Mach stem are almost unchanged, with a value of approximately $H_m/H_\infty = 0.282$. This is close to the numerical simulation of Shirozu & Nishida (1995) and the analytical result of Li & Ben-Dor (1997), which are both $H_m/H_\infty = 0.27$ in this test case. A comparison of the shapes of the Mach stem obtained from the present numerical simulation (with $\Delta x/L = 0.0025$) and predicted by the analytical formulation (46) using the heights

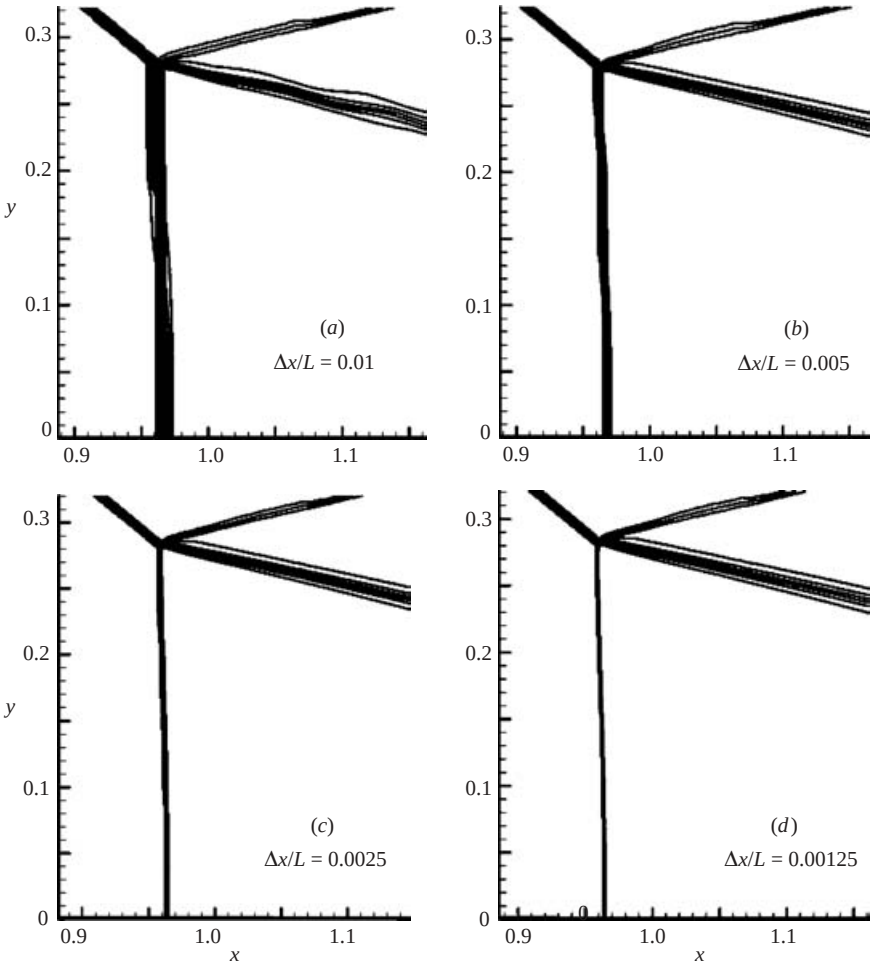

FIGURE 10. Mach number contours showing the shapes of Mach stem in the grid refinement study. $M_\infty = 4.96$, $\theta_w = 28.0°$, $w/H_\infty = 1.1$.

of the Mach stem determined by the present simulation and the analytical result of Li & Ben-Dor (1997) is shown in figure 13. The agreement is very good except at the upper end points of the Mach stem, where the computed Mach stem merges with the slipline. The discrepancy reflects the influence of the slipline due to the present Mach stem shape acquisition algorithm. Because of this close agreement, we believe that a grid of $\Delta x/L = 0.0025$ is sufficient for a quantitative comparison between the numerical and analytical shapes of the Mach stem.

Three additional test cases are presented now. The grid densities near the Mach stem are all similar to the grid with $\Delta x/L = 0.0025$ used in the grid refinement study. The flow conditions corresponding to these test cases are summarized in table 1. The average errors between the numerical and analytical Mach stems are shown in table 2. These errors are measured in terms of the difference between the analytical and computed horizontal locations of the shock wave, and are normalized by the horizontal shift of the Mach stem $D = H_m(\alpha/\theta_3 - \sqrt{(\alpha/\theta_3)^2 - 1})$. The comparison between the numerical results and the analytical shapes is displayed in figure 14 to figure 16 for the test cases presented in table 1. It is seen that the agreement between

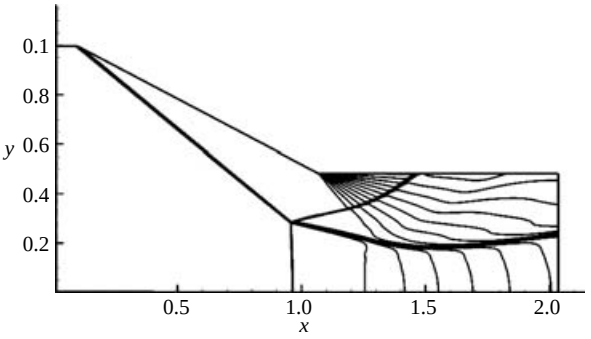

FIGURE 11. Mach number contours corresponding to the finest grid in the grid refinement study. $M_\infty = 4.96$, $\theta_w = 28.0°$, $w/H_\infty = 1.1$, $\Delta x/L = 0.0025$.

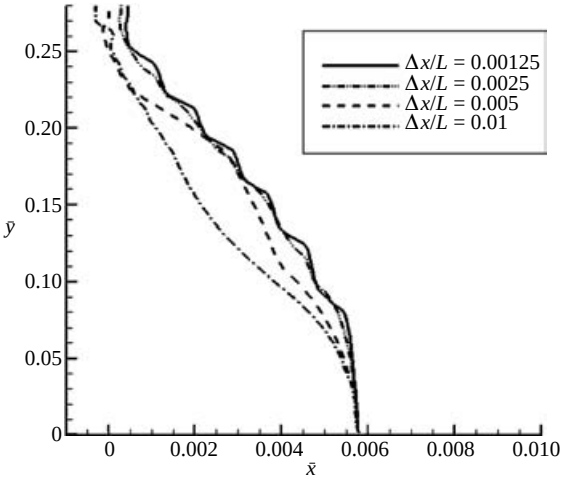

FIGURE 12. Shapes of the Mach stem in the grid refinement study. $M_\infty = 4.96$, $\theta_w = 28°$, $\theta_3 = 12.03°$.

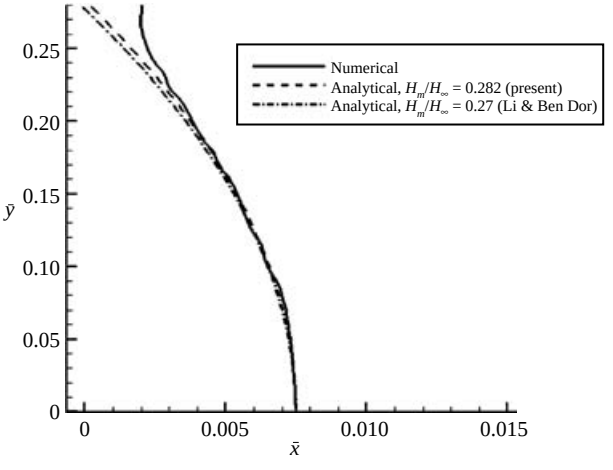

FIGURE 13. Comparision of the shapes of the Mach stem obtained from the present numerical simulation and predicted by the analytical formulation (46) using the heights of the Mach stem determined by the present simulation and the analytical result of Li & Ben-Dor (1997). $M_\infty = 4.96$, $\theta_w = 28°$, $\theta_3 = 11.03°$, $\Delta x/L = 0.0025$.

	Case I (figure 14)	Case II (figure 15)	Case III (figure 16)
θ_w	21.846°	24°	26°
M_∞	3.0	3.0	3.0
w/H_m	1.4	1.0	0.7
θ_3	4.20°	8.43°	12.48°

TABLE 1. The flow conditions for the three additional test cases.

	Case I	Case II	Case III
$\dfrac{\lvert x_{analytical} - x_{numerical}\rvert_{average}}{D}$	5.5 %	3.1 %	3.0 %

TABLE 2. Errors between the theory and the numerical results for the three additional test cases.

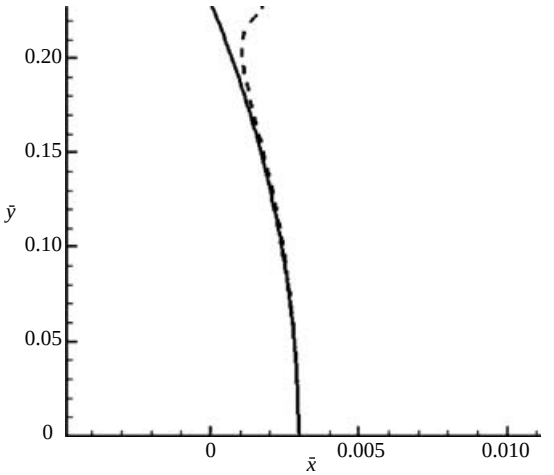

FIGURE 14. The analytical and the computed shapes of the Mach stem when $\theta_w = 21.846°$, $M_\infty = 3.0$, $\theta_3 = 4.20°$ and $w/H_\infty = 1.4$. The solid line is the analytical result, and the dashed line is the numerical result.

the simulated and analytical shapes of the Mach stem is very good. The largest error among these test cases is 5.5 %.

4.3. *Discussion*

Because of the close agreement between the analytical and simulated shapes of the Mach stem, (46) can be used to quantitatively describe the shapes of the Mach stem. Below are some further remarks.

(i) Equation (46) can be normalized to obtain

$$\left(\hat{x} + \sqrt{\left(\frac{\alpha}{\theta_3}\right)^2 - 1}\right)^2 + \hat{y}^2 = \left(\frac{\alpha}{\theta_3}\right)^2, \tag{49}$$

where $\hat{x} = x/H_m$ and $\hat{y} = y/H_m$. Solving for $\hat{x}$ using (49) yields

$$\hat{x} = \frac{\alpha}{\theta_3}\left(\sqrt{1 - \left(\frac{\theta_3 \hat{y}}{\alpha}\right)^2} - \sqrt{1 - \left(\frac{\theta_3}{\alpha}\right)^2}\right).$$

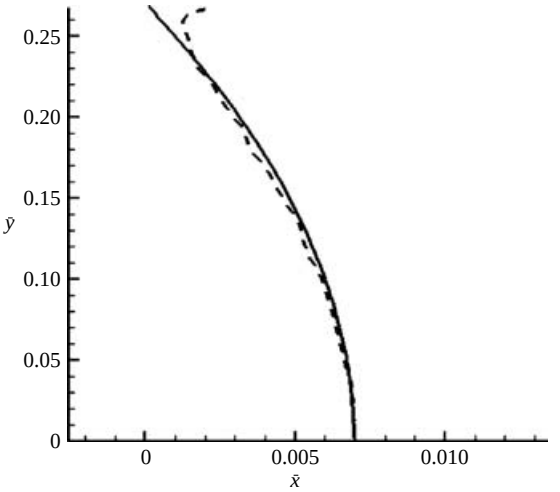

FIGURE 15. As figure 14 but for $\theta_w = 24°$, $M_\infty = 3.0$, $\theta_3 = 8.43°$ and $w/H_\infty = 1.0$.

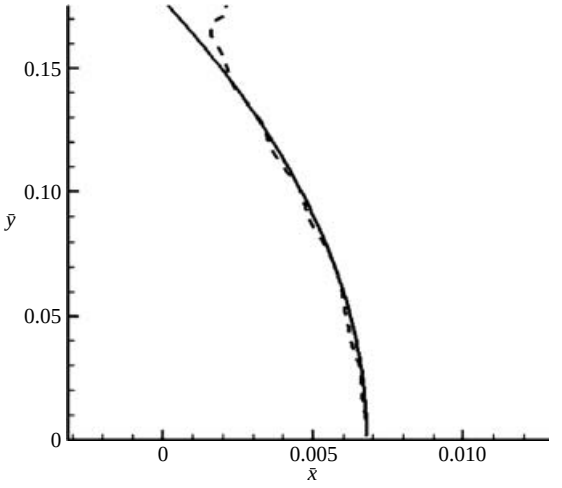

FIGURE 16. As figure 14 but for $\theta_w = 26°$, $M_\infty = 3.0$, $\theta_3 = 12.48°$ and $w/H_\infty = 0.7$.

Since both $\theta_3\hat{y}/\alpha$ and θ_3/α are small quantities, the use of Taylor's expansion leads to

$$\hat{x} = \frac{\theta_3}{2\alpha}(1 - \hat{y}^2). \tag{50}$$

Now we compare this expression with the one given by Li & Ben-Dor (1997). Using the coordinate system and notation of the present paper, the formulation of Li & Ben-Dor (1997) can be expressed as

$$\hat{x} = \frac{\cot(\beta_3)}{2}(1 - \hat{y}^2), \tag{51}$$

where β_3 is the shock angle β at the triple point satisfying

$$\tan\theta_3 = 2\cot\beta_3 \frac{M_\infty^2 \sin^2\beta_3 - 1}{M_\infty^2(\gamma + \cos 2\beta_3) + 2}$$

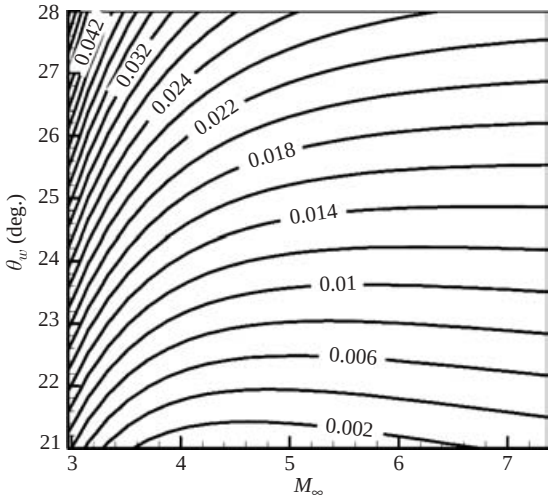

FIGURE 17. The contour lines of D/H_m showing the dependence of D/H_m on M_∞ and θ_w.

(see (3)). For small θ_3 and $\beta - \pi/2$, we have

$$\cot\beta_3 \approx \frac{\theta_3}{\dfrac{2(M_\infty^2-1)}{M_\infty^2(\gamma-1)+2}} = \frac{\theta_3}{\alpha}.$$

Therefore, (50) and (51) are in fact identical for small values of θ_3 and $\beta - \pi/2$.

(ii) The normalized horizontal shift of the Mach stem is $D/H_m = \alpha/\theta_3 - \sqrt{(\alpha/\theta_3)^2 - 1}$ according to (46). Since θ_3/α is a function of M_∞ and θ_w, the normalized horizontal shift of the Mach stem is also related to M_∞ and θ_w. Using the three-shock theory, the relation between D/H_m and M_∞ and θ_w is illustrated in figure 17. It is clear that D/H_m is an increasing function of θ_w for the same value of M_∞. The dependence of D/H_m on the incoming-flow Mach number, M_∞, is not monotonic: for a fixed θ_w, D/H_m at first increases with M_∞; and after a critical value of M_∞, decreases with increasing M_∞.

(iii) We now discuss the factors affecting the shape of the Mach stem. We know that θ_3/α is a function of M_∞ and θ_w,

$$\frac{\theta_3}{\alpha} = g(M_\infty, \theta_w).$$

According to (49) or (50), the normalized Mach stem shape can be determined by M_∞ and θ_w. Hornung & Robinson (1982) have pointed out that

$$H_m/w = f(\gamma, M_\infty, \theta_w, H_t/w),$$

where H_t is the height of the trailing edge of the wedge. Therefore, the shape of the Mach stem is determined by the specific heats ratio, the incoming-flow Mach number, and the geometrical set-up parameterized by w, H_t and θ_w.

5. Summary

In this paper, a detailed analysis of the subsonic flow pocket just behind the Mach stem is performed by assuming the angle between the slipline and the reflecting plane to be small. Under this assumption, the features of flow field in this region are

analysed and an analytical expression for the shape of the Mach stem is obtained. The main conclusions of the present paper are summarized below.

(*a*) For a wide range of flow conditions M_∞ and θ_w, the deviation angle θ_3 of the slip-line is small. For instance, when $M_\infty = 3.0 \sim 5.0$ and $\theta_w = 21^\circ \sim 28^\circ$, θ_3 is less than 12° (0.209 rad) except at the upper left corner of the (M_∞, θ_w) diagram, see figure 4.

(*b*) In the subsonic region that just behind the Mach stem, the perturbation flow field can be characterized by the following estimations of the perturbation variables:

$$\begin{aligned} s \sim O(\epsilon^2), \quad & \frac{\partial s}{\partial x} \ll \frac{\partial s}{\partial y}; \\ v_x \sim O(\epsilon^2), \quad & v_y \sim O(\epsilon); \\ \frac{\partial v_x}{\partial x} \sim O(\epsilon), \quad & \frac{T_0}{V_0}\frac{\partial s}{\partial x} \ll \frac{\partial v_x}{\partial x}. \end{aligned}$$

(*c*) The order estimations of the perturbation variables mentioned previously imply that the flow in this region can be described by the isentropic small-disturbance equation

$$(1 - M_0^2)\frac{\partial^2 \phi}{\partial x^2} + \frac{\partial^2 \phi}{\partial y^2} = 0,$$

which leads to an analytical expression for the shape of the Mach stem as follows:

$$\left(x + \sqrt{\left(\frac{\alpha H_m}{\theta_3}\right)^2 - H_m^2}\right)^2 + y^2 = \left(\frac{\alpha H_m}{\theta_3}\right)^2,$$

where

$$\alpha = \frac{2(M_\infty^2 - 1)}{2 + (\gamma - 1)M_\infty^2}.$$

(*d*) The shape of the Mach stem is a circular arc centred at

$$\left(-\sqrt{\left(\frac{\alpha H_m}{\theta_3}\right)^2 - H_m^2}, 0\right),$$

and the two end points are $(0, H_m)$ and $(\alpha H_m/\theta_3 - \sqrt{(\alpha H_m/\theta_3)^2 - H_m^2}, 0)$. For small θ_3 and $\beta - \pi/2$, this expression is identical to the shape expression obtained by Li & Ben-Dor (1997) using geometrical considerations.

(*e*) Numerical simulation using the full set of nonlinear Euler equations validates the analytical model. The numerical results are in good agreement with the theory in terms of the orders of the perturbation variables as well as the shapes of the Mach stems.

(*f*) As noted in § 1, Dewey & McMillin (1985*a*, *b*) have experimentally observed the shape of the Mach stem of pseudo-steady reflections and found that the Mach stem can be described well by a circular arc. Although they dealt with pseudo-steady reflections, their results nevertheless support the findings of the present paper.

This work was supported by the research fund of the Laboratory of Computational Physics of IAPCM, and by Chinese NSF (Contract No. 10376016).

REFERENCES

Azevedo, D. J. & Liu, C. S. 1993 Engineering approach to the prediction of shock patterns in bounded high-speed flows. *AIAA J.* **31**, 83–90.

Ben-Dor, G. 1991 *Shock Wave Reflection Phenomena*. Springer.

Ben-Dor, G., Elperin, T. & Vasiliev, E. I. 2003 Flow Mach number induced hysteresis phenomena in the interaction of conical shock waves – a numerical investigation. *J. Fluid Mech.* **496**, 335–354.

Ben-Dor, G., Igra, O. & Elperin, T. 2001 *Handbook of Shock Waves*. Vol. I–III. Academic.

Ben-Dor, G., Ivanov, M., Vasiliev, E. I. & Elperin, T. 2002 Hysteresis processes in the regular reflection <-> Mach reflection transition in steady flows. *Prog. Aerospace Sci.* **38**, 347–387.

Chpoun, A., Passerel, D., Lengrand, J. C., Li, H. & Ben-Dor, G. 1994 Mise en evidence experimentale et numerique d'un phenomane d'hysteresis lors de la transition reflexion de Mach-reflexion reguliere. *Mecanique des Fluides/Fluid Mechanics, C. R. Acad. Sci. Paris* **319**, II, 1447–1453.

Chpoun, A., Passerel, D., Li, H. & Ben-Dor, G. 1995 Reconsideration of the oblique shock wave reflection in steady flows. Part 1. Experimental investigation *J. Fluid Mech.* **301**, 19–35.

Courant, R. & Friedrichs, K. O. 1948 *Supersonic Flow and Shock Waves*. Wiley-Interscience.

Dewey, J. M. & Barss, T. 1996 The shape of the Mach stem. *Proc. 12th Intl Mach Reflection Symp., Pilanesberg, South Africa*, pp. 263–274.

Dewey, J. M. & McMillin, D. J. 1985*a* Observation and analysis of the Mach reflection of weak uniform plane shock waves. Part 1. Observations. *J. Fluid Mech.* **152**, 49–66.

Dewey, J. M. & McMillin, D. J. 1985*b* Observation and analysis of the Mach reflection of weak uniform plane shock waves. Part 2. Analysis. *J. Fluid Mech.* **152**, 67–81.

Emanuel, G. 1986 *Gasdynamics: Theory and Applications*. AIAA.

Fomin, V. M., Hornung, H. G., Ivanov, M. S., Kharitonov, A. M., Klemenov, G. P., Kudryavtsev, A. N. & Pavlov, A. A. 1996 The study of transition between regular and Mach reflection of shock waves in different wind tunnels. *Proc. 12th Intl Mach Reflection Symp., Pilanesberg, South Africa*, pp. 137–151.

Henderson, L. F. & Lozzi, A. 1975 Experiments on transition of Mach reflection. *J. Fluid Mech.* **68**, 139–155.

Hendersin, L. F. & Lozzi, A. 1979 Further experiments on transition of Mach reflection. *J. Fluid Mech.* **94**, 541–559.

Hornung, H. G., Oertel, H. & Sandeman, R. J. 1979 Transition to Mach reflection of shock waves in steady and pseudo-steady flows with and without relaxation. *J. Fluid Mech.* **90**, 541–560.

Hornung, H. G. & Robinson, M. L. 1982 Transition from regular to MR of shock waves. Part 2. The steady flow criterion. *J. Fluid Mech.* **123**, 155–164.

Ivanov, M. S., Gimelshein, S. F. & Beylich, A. E. 1995 Hysteresis effect in stationary reflection of shock waves. *Phys. Fluids* **7**, 685–687.

Li, H. & Ben-Dor, G. 1996 Application of the principle of minimum entropy production to shock wave reflections. I. Steady flows. *J. Appl. Phys.* **80**, 2027–2037.

Li, H. & Ben-Dor, G. 1997 A parametric study of Mach reflection in steady flows. *J. Fluid Mech.* **341**, 101–125.

Li, H., Ben-Dor, G. & Han, Z. Y. 1994 Modification on the Whitham theory for analyzing the reflection of weak shock waves over small wedge angles. *Shock Waves J.* **4**, 41–45.

Mach, E. 1878 Uber den Verlauf von Funkenwellen in der Ebene und im Raume. *Sitzungsbr Akad Wiss Wien* **78**, 819–838.

von Neumann, J. 1943 Oblique reflection of shock. *Explos. Res. Rep.* 12. Navy Dept., Bureau of Ordinance, Washington, DC.

von Neumann, J. 1945 Refraction, intersection and reflection of shock waves. *NAVORD Rep.* 203–245 Navy Dept., Bureau of Ordinance, Washington, DC.

Olim, M. & Dewey, J. M. 1992 A revised three-shock solution for the Mach reflection of weak shocks ($1.1 < \mathrm{Mi} < 1.5$). *Shock Waves J.* **2**, 167–176.

Quirk, J. 1994 A contribution to the Great Riemann Solver Debate. *Intl J. Numer. Meth. Fluids* **18**, 555–574.

Ren, Y. X. 2003 A robust shock capturing scheme based on the rotated Riemann solver. *Computers Fluids* **32**, 1379–1403.

Shapiro, A. H. 1953 *The Dynamics and Thermodynamics of Compressible Fluid Flow*. John Wiley & Sons.

Shirozu, T. & Nishida, M. 1995 Numerical studies of oblique shock reflction in steady two-dimensional flows. *Memoirs Faculty Engng, Kyushu Univ*. **55**, 193–204.

Skews, B. W. 1997 Aspect ratio effects in wind tunnel studies of shock wave reflection transition. *Shock Waves* **7**, 373–383.

Skews, B. W. 2000 Three dimensional effects in wind tunnel studies of shock wave reflection. *J. Fluid Mech.* **407**, 85–104.

Teshukov, V. M. 1989 On stability of RR of shock waves. *Prikl. Mekh. i Techn Fizika* **2**, 26–33.

Vuillon, J., Zeitoun, D. & Ben-Dor, G. 1995 Reconstruction of oblique shock wave reflection in steady flows. Part 2. Numerical investigation. *J. Fluid Mech.* **301**, 37–50.